# Modeling the Transient Response of Tropical Convection to Mesoscale SST Variations

ERIC D. SKYLLINGSTAD, SIMON P. DE SZOEKE, AND LARRY W. O'NEILL

*College of Earth, Ocean, and Atmospheric Sciences, Oregon State University, Corvallis, Oregon*

(Manuscript received 9 March 2018, in final form 7 February 2019)

ABSTRACT

A cloud-resolving model coupled to a mixed layer ocean with an initial 500-km-wide, +3-K sea surface temperature (SST) patch is used to demonstrate the relationship between tropical mesoscale SST gradients and convection under different wind speeds. On these scales, boundary layer convergence toward hydrostatic low surface pressure is partially responsible for triggering convection, but convection subsequently organizes into cells and squall lines that propagate away from the patch. For strong wind ($12\,m\,s^{-1}$), enhanced convection is shifted downstream from the patch and consists of relatively small cells that are enhanced from increased moist static energy (MSE) flux over the patch. Convection for weak wind ($6\,m\,s^{-1}$) develops directly over the patch, merging in larger-scale coherent squall-line systems that propagate away from the patch. Squall lines decay after approximately 1 day, and convection redevelops over the patch region after 2 days. Decreasing patch SST from ocean mixing in the coupled simulations affects the overall strength of the convection, but does not qualitatively alter the convective behavior in comparison with cases with a fixed 3-K SST anomaly. In all cases, increased fluxes of heat and moisture, along with latent heating from shallow convection, initially generate lower pressure over the patch and convergence of the boundary layer winds. Within about 1 day, secondary convective circulations, such as surface cold pools, act to spread the effects of the convection over the model domain and overwhelm the effect of low pressure. SST anomalies (1 and 0.5 K) generate enhanced convection only for winds below $6\,m\,s^{-1}$.

## 1. Introduction

Tropical convection can range in scales from individual cells less than 10 km in size to large-scale disturbances spanning thousands of kilometers, for example, the intertropical convergence zone (ITCZ) or intraseasonal Madden–Julian oscillation (MJO) events. For convective systems smaller than 500 km, satellite data suggest that sea surface temperature (SST) variability exerts some control on the local formation of convection and may play a role in determining the convective scale. Li and Carbone (2012, hereafter LC) showed a correlation between SST Laplacian and next-day precipitation from satellite-derived precipitation and SST. From these data, they hypothesized that the wind convergence linked to SST warm anomalies was the dominant mechanism for convective precipitation excitation. Their analysis, however, was unable to directly infer causation between the measured SST to wind convergence and enhanced convection. In the current study, we seek to understand the processes responsible for the correlations between SST and rain, by examining how changes in the marine boundary layer (MBL) associated with mesoscale variations in SST affect the formation and evolution of tropical convection over a period of 1–3 days in a cloud-resolving model coupled to an ocean mixed layer model with a prescribed initial SST field.

Mesoscale variability in SST affects surface heat fluxes, which then alters the boundary layer, leading to convective activity. At any given time, moist turbulent air in the boundary layer might penetrate the boundary layer inversion, leading to condensation and new convective clouds. Two conditions can make this process more likely: forced upward motion from surface wind convergence (convergence mechanism), and increased boundary layer moisture and/or heat content [moist static energy (MSE) mechanism]. Both of these conditions can be produced or enhanced by mesoscale

Denotes content that is immediately available upon publication as open access.

*Corresponding author*: Eric D. Skyllingstad, skylling@coas.oregonstate.edu

DOI: 10.1175/JAS-D-18-0079.1

variations in SST. For example, over regions of warmer SST, the nearly hydrostatic surface pressure is less than over the surrounding water because of the lower density of the warmer and moister boundary layer (Lindzen and Nigam 1987; Hsu 1984; Cronin et al. 2003; Hashizume et al. 2002). Lower surface pressure generates convergent surface winds and upward motion over the warm SST, depending on the strength of the background wind, rotation, and size of the warm water patch (Lindzen and Nigam 1987). The thermally induced surface pressure response to SST is somewhat mitigated by compensating temperature changes of opposite sign from a higher inversion (e.g., Hashizume et al. 2002). The boundary layer wind convergence is related to the Laplacian of SST, with modifications due to planetary rotation.

In addition to the effects of convergence, anomalously warm SST generates MSE and greater convective instability. Both convergence and surface MSE flux are strongly affected by increasing the ambient wind speed. Winds also change the SST through increased heat loss and entrainment of cooler water at the ocean mixed layer base. Wind speed will be shown to play a critical role in modulating the effectiveness of warm SST in modifying convective forcing.

Quantifying these processes over the ocean is difficult because the vertical structure of winds and temperature in the MBL is not routinely measured. Satellite winds can provide reasonable surface divergence estimates; however, accurate SST data at high enough spatial and temporal resolution are frequently missing in regions of convection because of the cloud cover and precipitation. It could be that the correlation LC detected between rainfall and Laplacian of SST results not from wind convergence, but instead from increased moist static energy over the warm patch [similar to the interpretation given in Carbone and Li (2015) for MJO events]. While the mesoscale surface wind response to SST gradients can be explained by a number of processes (e.g., Lindzen and Nigam 1987; Hayes et al. 1989; Samelson et al. 2006), research on the convective response is much more limited. The mesoscale correlation between the SST Laplacian, convergence, and convective initiation does not resolve the ambiguity in physical mechanisms that couple SST and convection.

Determining how mesoscale SST variability controls new convective development through changes in surface convergence and/or MSE flux is the main objective of this study. We explore mechanisms that can generate enhanced convection in response to mesoscale SST features using a cloud-resolving large-eddy simulation (LES) model, described in section 2, with an idealized warm-SST-anomaly lower boundary condition and simple one-dimensional ocean mixed layer. Results from three sets of experiments are presented in section 3, suggesting that the proposed convective onset and enhancement mechanisms described above are strongly affected by the overall wind speed and strength of the imposed SST anomaly. In general, both boundary layer convergence and enhanced moist static energy control the development and behavior of convection in response to SST anomalies, but with background wind speed strongly modifying the convective behavior. A conceptual model based on convective cold pool propagation is described in section 4 and the paper is concluded in section 5.

## 2. Model and experiments

### a. Model setup

Simulations are conducted using the cloud-resolving large-eddy simulation model described in Skyllingstad and de Szoeke (2015). This model is based on the Deardorff (1980) dynamical equations with turbulence closure based on a Smagorinsky approach following Mason (1994). Radiative transfer is parameterized using the Rapid Radiative Transfer Model (Mlawer et al. 1997). Cloud microphysics are modeled using a seven-component scheme developed by Thompson et al. (2008). Scalar transport in the model is performed using a positive definite, mass-conserving van Leer method based on Colella (1990). Pressure is calculated with a time-split compressible scheme with an implicit vertical term following Wicker (2009). A simple, mixed layer ocean model using the $K$-profile parameterization (Large et al. 1994) is applied at each model grid point with surface fluxes determined using the version 2.5 COARE bulk method as implemented by Vickers and Mahrt (2006). A domain size of 2560 km $\times$ 1280 km was selected that was sufficiently large to allow for multiple convective cells and SST variability on ~100-km scales. We chose a channel configuration with 1280 grid points in the zonal direction and 640 grid points in the meridional direction with a horizontal resolution of 2 km. In the vertical, 100 levels were used with a variable spacing starting with 10 m at the surface and gradually increasing to a constant 150 m at 1.5-km height. Above 15-km height, the vertical grid spacing was increased further using a sinusoidal function to a maximum of 450 m at 22 km. Periodic boundaries were applied in both horizontal directions with a rigid lid at the model top above a sponge zone extending over one-fifth of the upper model grid points.

Model initial conditions were prescribed by average profiles measured over the tropical Indian Ocean at

0°, 80.5°W from the R/V *Revelle* during the Dynamics of the Madden–Julian Oscillation (DYNAMO) field experiment in 2011 (Johnson and Ciesielski 2013). Conditions during this experiment were broadly representative of the tropical marine environment with a nearly moist adiabatic temperature structure above ~3-km height and a dewpoint temperature depression increasing with height from values of about 4°–5°C in the marine boundary layer. Winds in the model were initialized at a constant westerly value and maintained in geostrophic balance for a latitude of 5°N with a constant Coriolis parameter.

Ocean initial conditions were prescribed using an idealized ocean profile similar to observations from the DYNAMO (e.g., Moum et al. 2014). Initial SST was set in the model to a fixed value of $SST_{init} = 30°C$ with an elliptical patch of warm water in the center of the domain defined as

$$SST = SST_{init} + 0.5\Delta T\left\{1 - \tanh\left[\frac{(r - y_c/6)}{W}\right]\right\}, \quad \text{where}$$

$$r = \sqrt{\left[\frac{(x_c - x)}{2}\right]^2 + (y_c - y)^2},$$

where $x$ is the zonal coordinate, $y$ is the meridional coordinate, $y_c = 640$ km and $x_c = 1280$ km are the center of the domain, $\Delta T$ is the SST patch temperature anomaly, and $w = 60$ km sets the horizontal scale of the SST gradient (Fig. 1). The SST anomaly was extended downward to a depth of 10 m with a smooth transition over depth to the background temperature at roughly the mixed layer base at 20 m. The prescribed SST patch was thus representative of a region of enhanced solar warming and weak entrainment within a ~20-m mixed layer, such as would be observed in the tropical warm pool after many days of relatively clear skies and weak wind.

In all experiments, the atmospheric model was spun up for 1 day with a lower boundary condition of uniform SST set to the average SST value (including the warm anomaly). Mixing of the ocean was permitted during this spinup using the local gridpoint calculated fluxes, resulting in a decrease of the domain and patch temperature. Three-day coupled simulations were then conducted using the modified SST following the spinup period. All time references exclude the spinup period. Solar radiative fluxes are representative of 2°N, 80°E, with the initial time set to 0000 UTC or about 0600 LST. The tropospheric temperature profile is typically cooling at the beginning of the simulation. It approaches radiative–convective equilibrium by the end of the 3-day simulation as convective heating balances longwave radiative flux divergence. Average SST in the model is gradually changing over the model period indicating that full radiative–convective equilibrium is not achieved over the short simulation period. In addition to the coupled experiments, a set of fixed-SST warm patch cases were conducted to evaluate the effects of SST change on convective behavior.

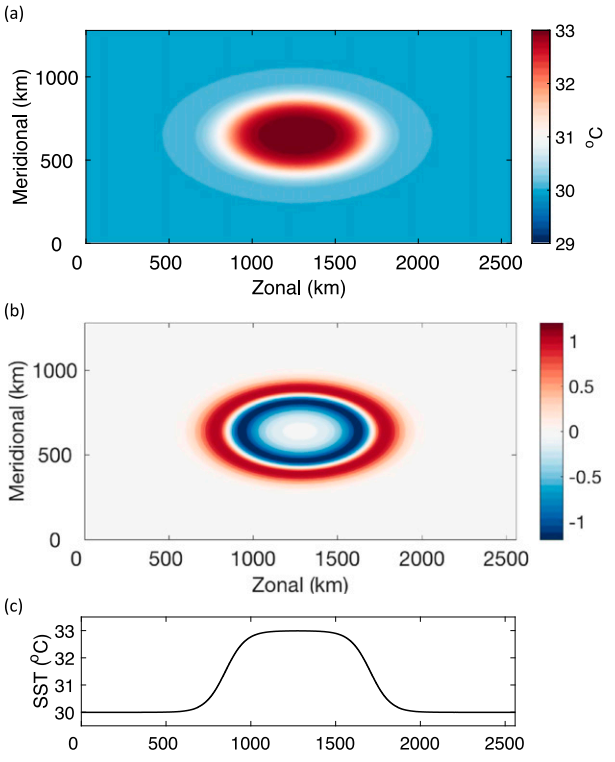


FIG. 1. (a) Initial ocean sea surface temperature for $\Delta T = 3°C$, (b) Laplacian of SST (°C m$^{-2}$), and (c) cross section of SST along the centerline of the domain.

## b. Experiments

Three sets of experiments were conducted using the above model setup:

1) Our first set of experiments examines how convection forms in response to different background wind speeds for a set initial SST $\Delta T = 3°C$ that varies through model coupling. Satellite observations presented in LC suggest that convective systems triggered by mesoscale SST variability are typically downwind from warm SST patches and more common during weak wind conditions. Our experiments determine the underlying processes responsible for establishing convective activity and the role of ambient wind speed in controlling the location and evolution of convective organization in response to the warm SST patch evolution. Geostrophic background winds

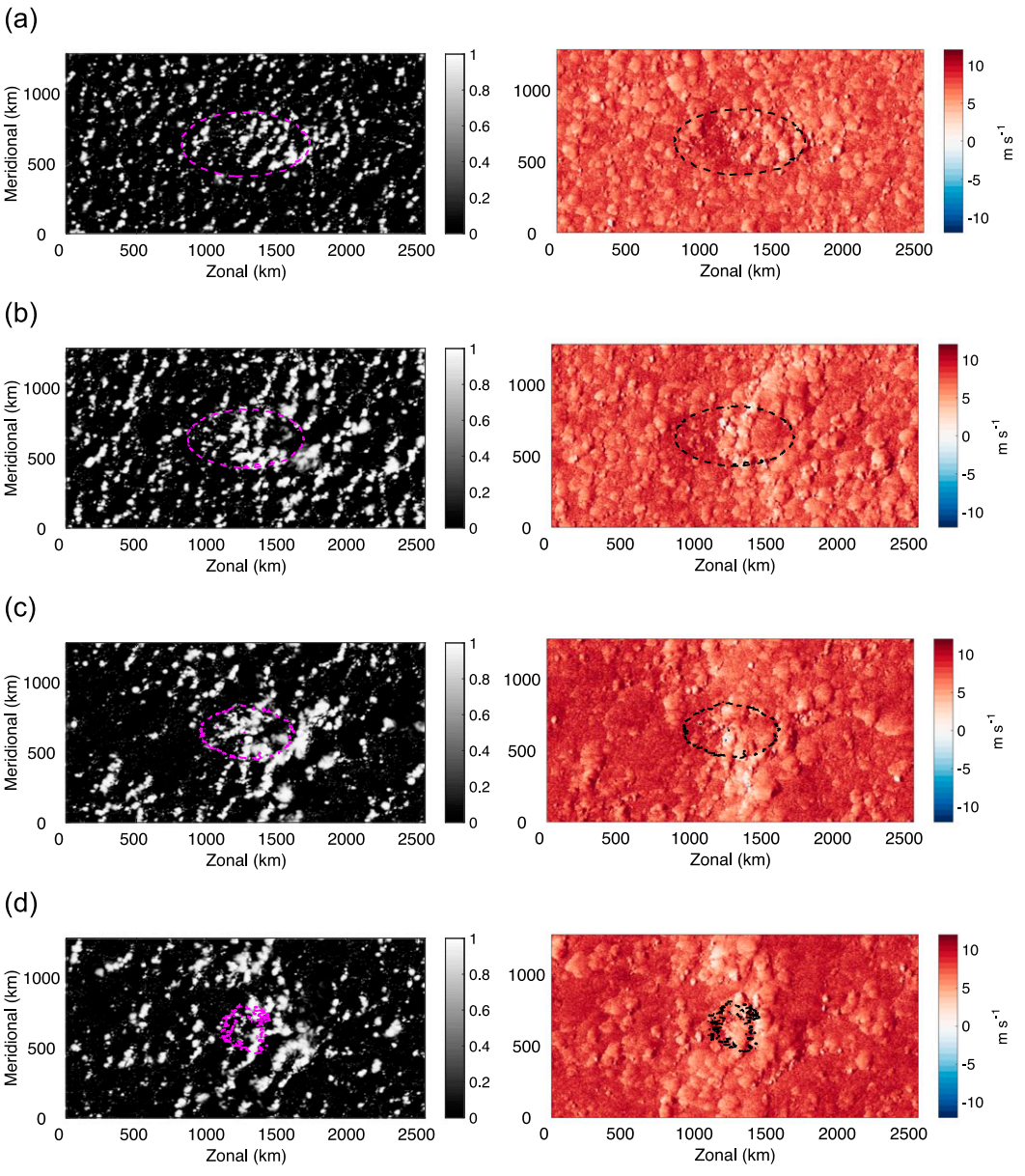


FIG. 2. (left) Simulated cloud albedo and (right) surface $u$-wind component for case U12 at (a) hour 12 and at the end of days (b) 1, (c) 2, and (d) 3. The single dashed contour represents an SST value of 31°C.

of 6 and 12 m s$^{-1}$ are prescribed for these experiments, designated as cases U6 and U12, respectively. Shear is expected to have a strong effect on convective organization. We purposely did not experiment with the background wind shear in any of our experiments. Cases with uncoupled, fixed SST patch temperature (U6F and U12F) are also considered.

2) The second set of experiments decomposed the effects of turbulent surface fluxes on convective development. In these cases, we apply the same wind conditions as our first experiment set, but remove the spatial variability alternately in the surface sensible heat flux or the surface latent heat flux by applying the respective domain-average surface flux over the entire lower boundary. The ocean in these cases is forced by the local flux and not the domain average. Experiments with spatially averaged surface latent or sensible heat flux are identified by appending AL or AS, respectively, to the case name.

3) A final set of experiments is conducted to test the hypothesis that convective initiation is sensitive to

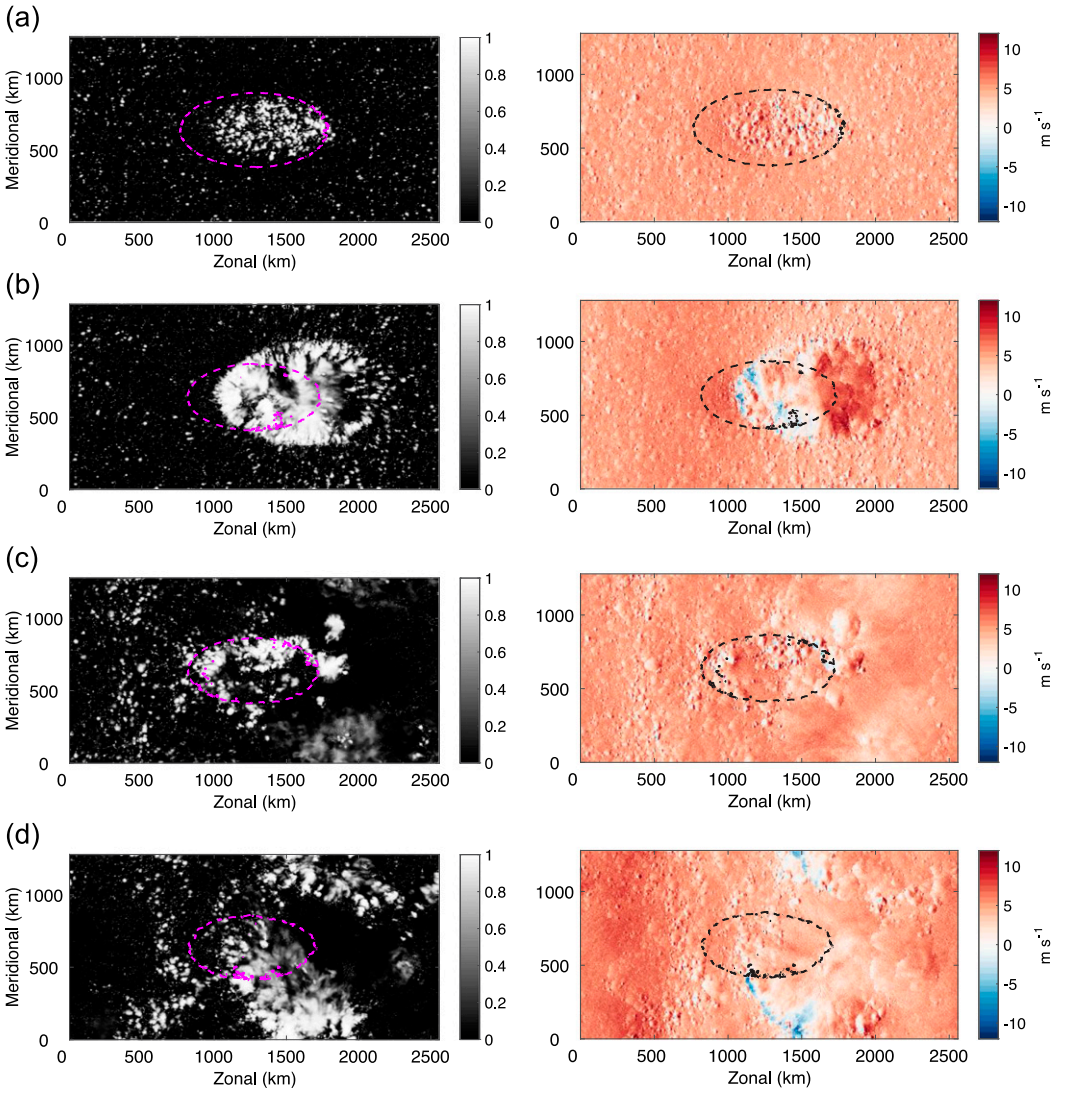


FIG. 3. As in Fig. 2, but for case U6.

relatively small SST variations for conditions with low ambient background winds. Three cases are considered, one with SST $\Delta T = 1°C$ and winds of $U = 6\,m\,s^{-1}$ (case U6-1), a second with winds of $12\,m\,s^{-1}$ and a fixed SST $\Delta T = 1°C$ (case U12-1F), and a third with $\Delta T = 0.5°C$ and $U = 3\,m\,s^{-1}$ (case U3).

## 3. Results

### a. *Effects of wind speed*

We present plots of the simulated cloud albedo and surface zonal wind for cases U12 (Fig. 2) and U6 (Fig. 3). Convective enhancement in both simulations is initially located near the SST patch. In case U12, convective cells are concentrated on the downwind side of the patch center and form a loose aggregation that slowly propagates upwind over the 3-day simulation time period (Fig. 2). The influence of the patch in this case tends to generate larger convective cells located directly over the warmest water after the initial development, with stronger cells also forming in a band centered over the patch, but not necessarily directly over the warmer water. Convective organization is controlled by internal dynamics of the storm systems; local SST appears to have an indirect effect on the location and strength of new cells. For example, on day 3 relatively strong convective cells are distributed both over and to the sides of the patch over cooler SST.

In the lower-wind case (U6), the effects of the warm patch are initially more focused with the formation of a cloud cluster over the patch that propagates meridionally before dissipating around day 3 (Fig. 3).

Convection in this case behaves more like an organized squall line with a band of strong surface winds moving outward from the SST patch forming a region of surface divergence. Convective cold pools are the source of these winds along with cooler surface air temperatures and enhanced precipitation, consistent with observed tropical convective cold pool systems (Kilpatrick and Xie 2015; de Szoeke et al. 2017). Although the initial convective cluster appears attached to the SST patch, after 2 days the squall line propagates north and south, again suggesting that the increased fluxes provided by the warmer water do not directly control convection after initially triggering the convection in the formation period. For both the U12 and U6 cases, convection is not anchored over the maximum Laplacian of SST, which occurs on the flanks of the maximum SST (see Fig. 1). Instead, cells tend to form over the warmest water. Later they propagate away from the patch as storm dynamics dominate the circulation.

Wind variations in case U12 initially are tied to the downstream convective development, but ultimately form a large-scale perturbation that extends across the domain in a north–south orientation (Fig. 2c). Cross-sectional plots (Fig. 4) suggest that this disturbance is a convectively forced internal wave circulation similar to westward-propagating ''gust fronts'' described in Tulich and Mapes (2008). They point out that these deep internal wave modes are forced by midlevel latent heat release and are distinct from cold pool density currents. Over time, the deceleration of surface velocity associated with the internal waves behaves as a coherent flow disturbance extending meridionally across the domain with a slow eastward propagation. Vertical temperature perturbations shown in Fig. 4b for case U12 are consistent with the internal wave mode discussed in Tulich and Mapes (2008), which have multiple nodes in the vertical.

Wind and convective forcing produces cooling via surface fluxes and ocean mixed layer deepening as shown by plots of the SST (Fig. 5). In both cases, ocean mixing and surface flux forcing during the 24-h spinup period reduces the relative SST anomaly and generates average cooling. Overall, cooling is greater in case U12 because of increased winds producing a colder ocean after spinup in comparison with case U6. Over the duration of the simulation, the warm patch intensity in case U12 decreases from about 2° to 1°C. Cooling in case U6 is weaker overall, with the patch $\Delta T$ decreasing from about 3° to 2°C. The effects of increased cloud cover and small rain puddles in case U6 are also evident as shown by the patches of cooler SST in areas of active convection. We note that SST shown in Fig. 5a is at the peak of solar heating, which tends to elevate the temperature uniformly over the domain.

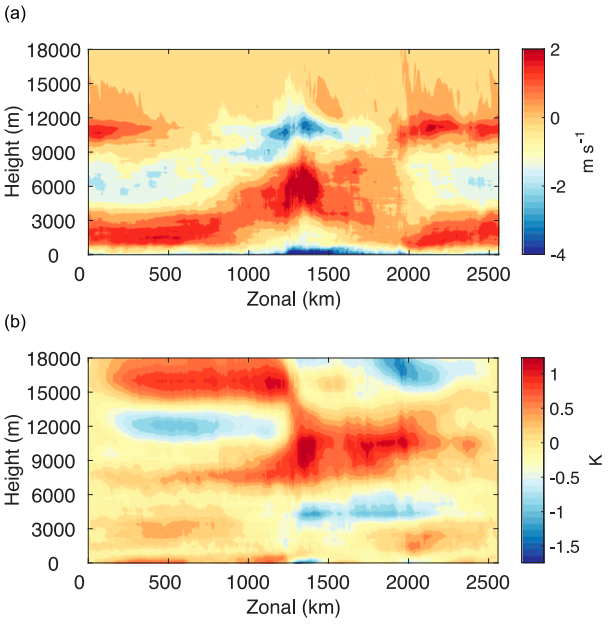


FIG. 4. Vertical cross sections along $y = 640$ km of (a) zonal wind perturbation from the prescribed 12 m s$^{-1}$ initial state ($u = 12$ m s$^{-1}$) and (b) perturbation temperature from 15-min snapshots averaged over 12 h, beginning on day 2 for case U12.

Hovmöller plots (time–zonal) show how the two cases differ in both convective strength and propagation character (Fig. 6). In case U12 (left column), the nearly stationary pattern of enhanced convection is evident in all of the displayed fields with small cell sizes and relatively small clusters remaining near $x = 1300$ km. In contrast, U6 (right column) displays large-scale structures that are maintained for about 24–36 h. In particular, the squall-line system generates a large perturbation in the surface wind, temperature, and moisture field near $x = 1000$ km that propagates westward at about 2 m s$^{-1}$ before moving away from the domain center on day 2. A second squall line forms on day 3 with a similar propagation speed. Downwind from the squall line, regions of relatively dry air moving eastward at ~6 m s$^{-1}$ extend from the convective activity toward the model boundary. These plumes of relatively dry surface air are signatures of cold pools produced by convective downdrafts as cells dissipate. Because of the squall-line and cold pool systems, the influence of convection in case U6 extends to distances larger than the SST patch.

In both cases, diurnal heating is evident in the surface temperature as shown by the weak banded structure coinciding with solar warming beginning just after the start of each simulated day. Convective cells also appear to have a slight diurnal signal with stronger cells during the nighttime period consistent with observations (Bellenger et al. 2010) and other modeling experiments (Liu and Moncrieff 1998).

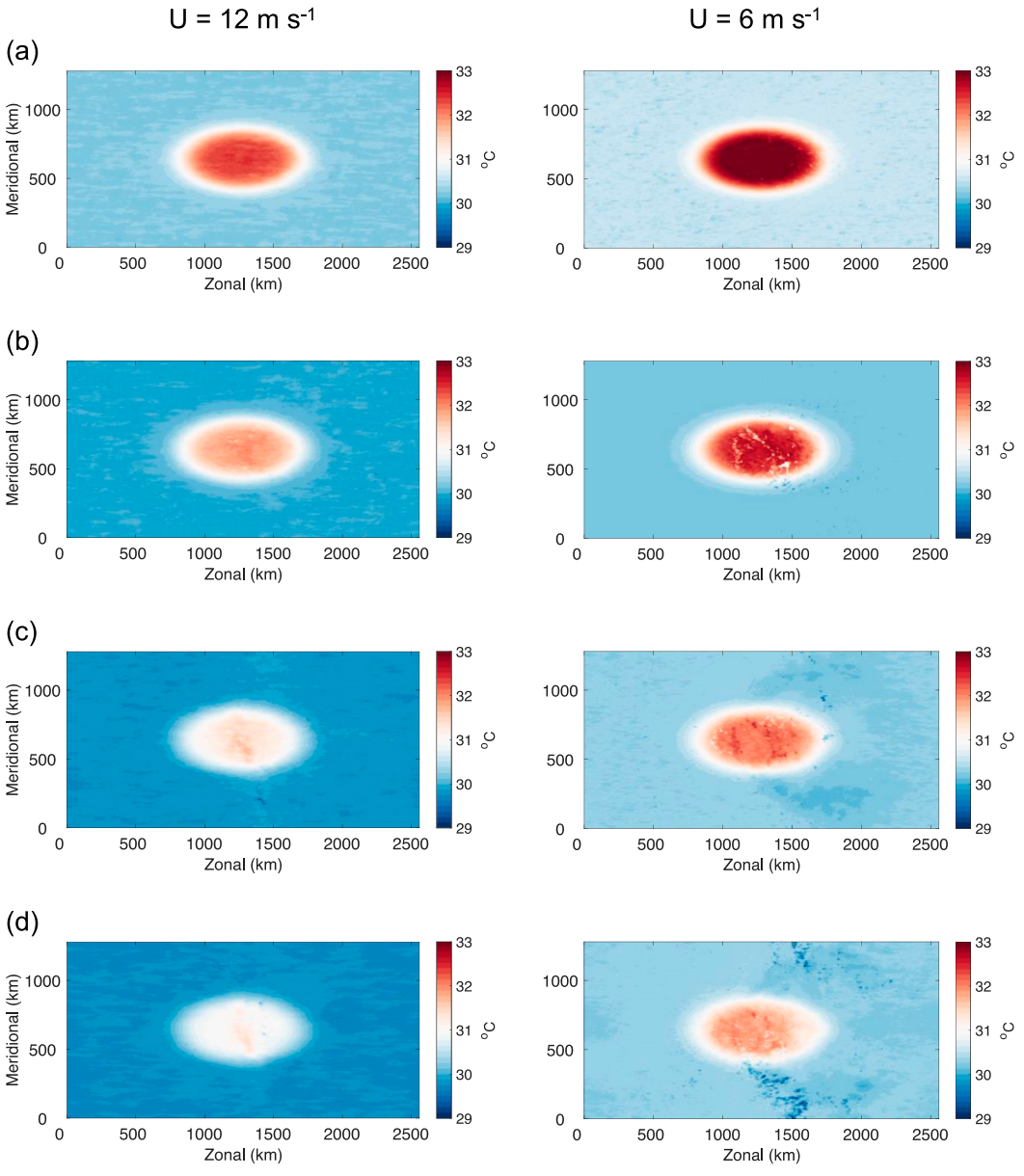


FIG. 5. Sea surface temperatures from cases (left) U12 and (right) U6 from hours (a) 12, (b) 24, (c) 48, and (d) 72.

Changes in the SST decrease the likelihood of convective redevelopment near the warm patch, but we believe are of secondary importance for overall convective propagation and strength until after the simulated 3-day period. The relatively deep (10 m) ocean mixed layer for these experiments was prescribed to ensure a robust convective response. Experiments with patch anomaly SST held constant at 3°C shown in Fig. 7 demonstrate that the changes in SST are not responsible for the basic convective response to the two wind speeds. For example, in case U6F, squall lines develop and propagate with roughly the same speed and location as in the coupled case. Likewise, in case U12F enhanced convection is relatively stationary over and downstream from the patch, similar to case U12 shown in Fig. 5 but with stronger convection. We plan to investigate the role of the ocean mixed layer depth on convection more completely in future research.

### b. *Surface flux sensitivity*

Cases U6 and U12 are examined with the average latent heat (cases U6AL and U12AL) and average sensible heat flux (cases U6AS and U12AS) applied uniformly over the surface. Surface flux averages

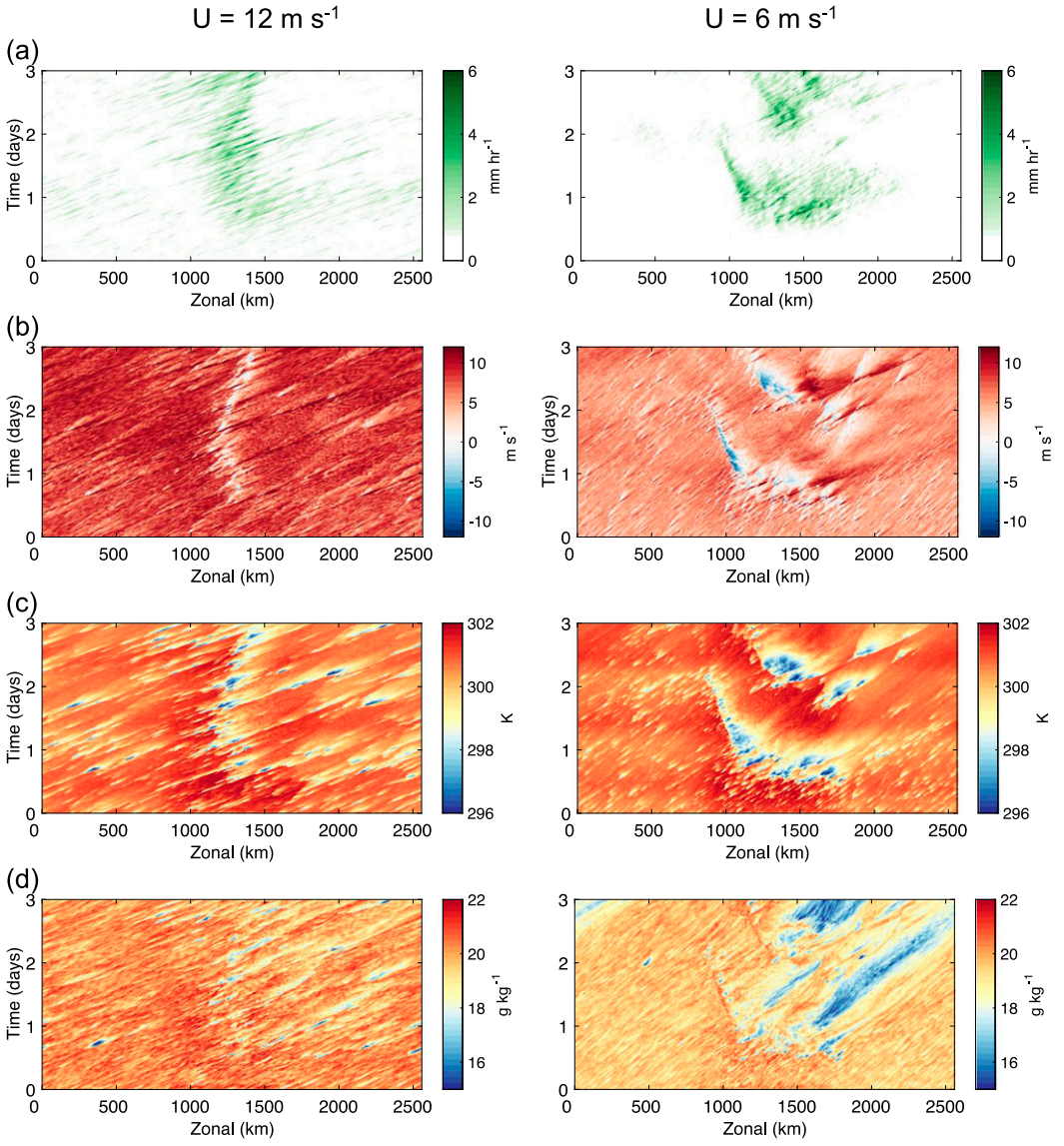


FIG. 6. Zonal direction–time sections for (a) meridional-average rainfall rate, (b) surface $u$ velocity component, (c) surface potential temperature, and (d) surface specific humidity. Surface values are taken from a section located at $y = 640$ km. Each day begins shortly before sunrise at 0600 LST.

are taken every time step. With average latent heat flux, the wind still responds to hydrostatic pressure associated with changes in the air temperature, but not to the ''virtual temperature'' effect of moisture on density generated by latent heat flux. Averaging the sensible heat flux removes most of the SST–wind coupling and isolates the influence of increased moisture flux over higher SST. We note that the upwelling longwave flux is about 18 W m$^{-2}$ higher over the warm patch because of increased surface-emitted infrared radiation.

Hovmöller plots of the meridional-average rainfall from each case shown in Fig. 8 demonstrate how the surface fluxes influence convective activity. Averaging the latent heat flux (U12AL) removes nearly all of the convective enhancement associated with the warm patch and internal wave coupling indicated by Fig. 6a. For case U12AS, convective enhancement over the SST patch is still apparent, but with lower intensity compared with the standard case shown in Fig. 6a. The decrease in convection in these two sensitivity experiments suggest that convective forcing is produced by both sensible and latent heat effects. Moisture flux and increased MSE is more important for stronger winds (case U12) than convergence due to boundary layer temperature gradients as shown by the large reduction in convection when latent heat flux is averaged.

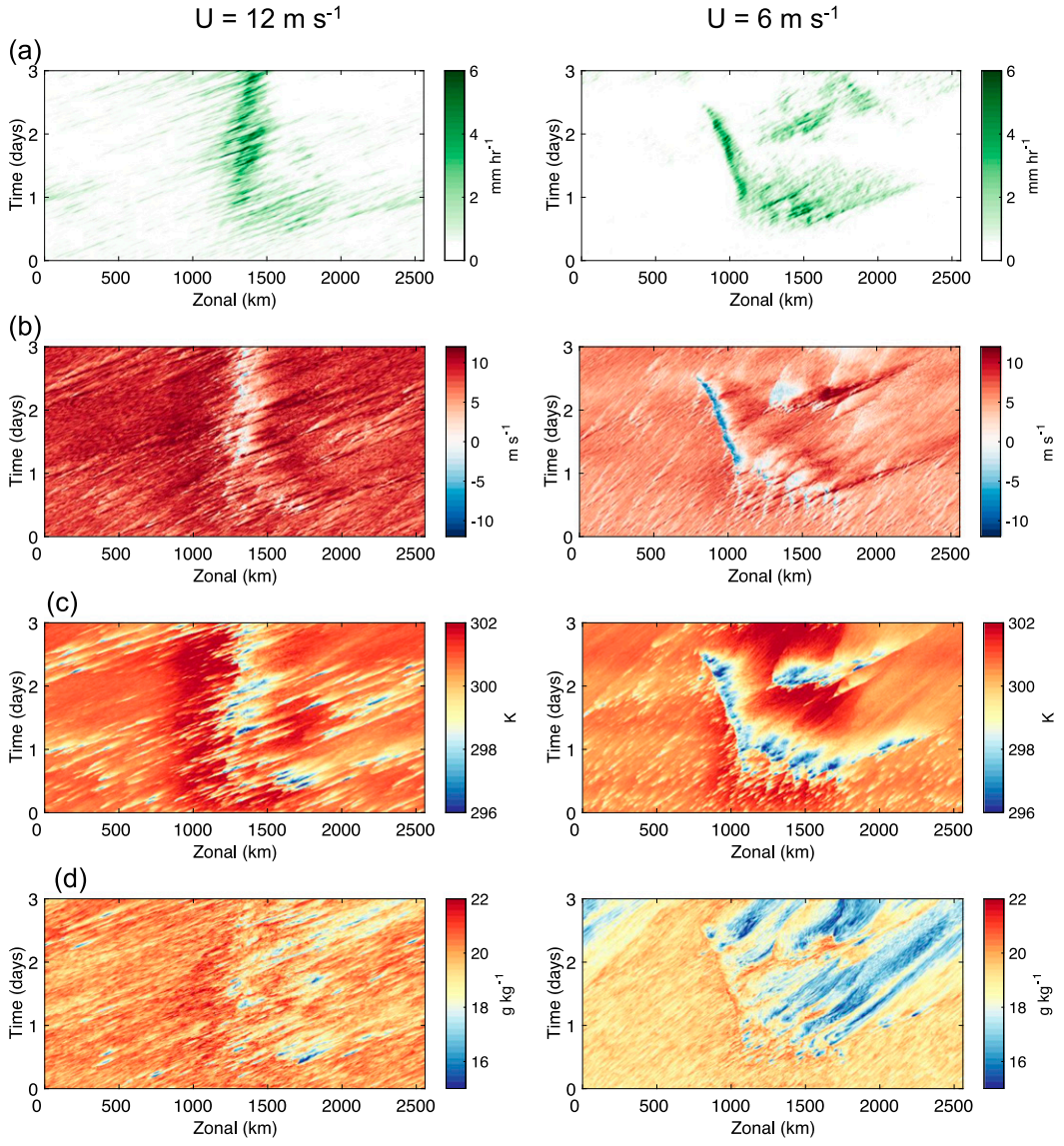


FIG. 7. As in Fig. 6, but with a fixed SST patch of $\Delta T = 3$°C.

Organized convection starts over the patch in all U6 simulations, suggesting that the local wind convergence associated with warmer SST (both direct and virtual temperature effects on density) is the dominant effect for lower wind speeds. We explore this hypothesis by focusing on the first 12 h of the warm patch simulation, before deep convection has formed.

The initial forcing is shown by plotting the surface pressure along with the average air temperature, specific humidity, and surface $u$ component of velocity during the first 12 h of day 1 as presented in Fig. 9 for case U6. Surface convergence shown in Fig. 9d results from lower pressure over the warm patch generated by the relatively warm and moist boundary layer produced through increased surface fluxes. In response to the lower pressure, winds tend to accelerate over the upwind side of the patch and decrease over the downwind side of the patch.

Corresponding plots from cases U6, U6AS, and U6AL showing the average fields between $y = 500$ and 780 km (Fig. 10) display similar patterns, with notable exceptions for moisture and temperature. Interestingly, the model produces a significant pressure perturbation in U6AS even though the temperature over the warm patch is about the same as the surrounding air mass (Fig. 10b). The virtual temperature effect (i.e., the effect of water vapor on the moist air density) in this case, along with a longwave flux heating and convective latent

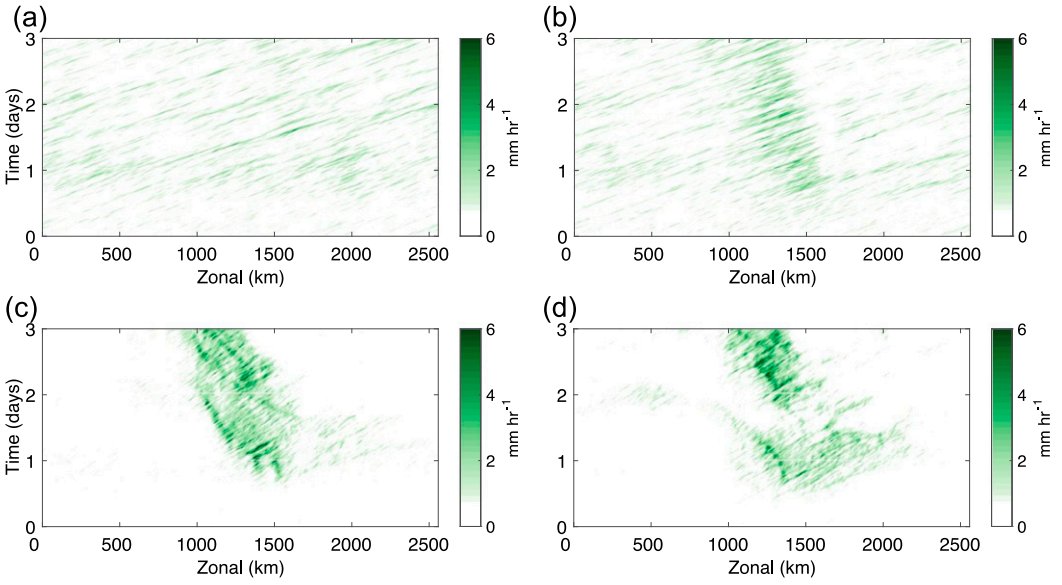


FIG. 8. Zonal direction–time sections of meridional-average rainfall rate for case (a) U12AL, (b) U12AS, (c) U6AL, and (d) U6AS.

heating aloft, continues to generate lower density and reduced surface pressure, thereby contributing to the formation of new convection along with the enhanced boundary layer moisture. The combined effect of these two terms explains roughly 50% of the total pressure perturbation over the warm patch. All cases have horizontal convergence roughly centered over the warm patch. We also note that the formation of shallow convection over the patch contributes to the reduced pressure through warming of the air aloft. This effect is shown more clearly below.

In the case with domain-averaged latent heat flux, higher temperature and lower pressure are observed as expected over the patch; however, lower specific humidity is somewhat surprising. We can explain this behavior by examining the boundary layer ($z < \sim 1000$ m) structure through cross sections centered on the patch in the east–west direction as shown in Fig. 11. The decrease in boundary layer moisture with case U6AL in comparison with U6 and U6AS results from the effects of sensible heat on boundary layer mixing. Greater sensible heat flux leads to increased turbulence and entrainment at the boundary layer top. The boundary layer heat budget is controlled mainly by the net flux of heat from the surface along with the entrainment heat flux, which both increase the boundary layer temperature. The entrainment flux also removes moisture from the boundary layer. When the surface sensible heat flux is averaged in AS, moisture is higher over the patch because the latent heat flux dominates weaker entrainment drying. However, when latent heat flux is averaged (AS), the surface source of moisture is reduced, but the entrainment flux at the boundary layer top remains the same as case U6. Entrainment dominates, decreasing boundary layer moisture. Increased boundary layer total kinetic energy (not shown) over the patch in case U6AL in comparison with case U6AS demonstrates increased mixing and drying from entrainment.

Further analysis of the vertical structure above the warm patch in case U6AS provides insight on determining which processes are responsible for the reduction in pressure over the patch region. In this case, pressure changes are primarily produced by the virtual effect from increased water vapor content and convective latent heating just above the boundary layer and between 4000 and 6000 m. These pressure changes are shown (Fig. 13) in both the modeled perturbation pressure and the integrated hydrostatic pressure. Negative density perturbations are noted both in the boundary layer from the virtual effect, and above the boundary layer from enhanced cloudiness (Fig. 12d). We note that removing the effects of surface SST on the longwave heating rates by using the domain-average SST for calculating the surface upwelling radiation has almost no effect on the perturbation density (not shown).

For comparison, plots of the perturbation density and pressure for case U6 show how increased sensible heat flux lowers the near-surface density, reducing the relative importance of virtual temperature and latent heating from convective clouds (Fig. 13). The initial pressure response to the warm patch in U6 is mostly confined to

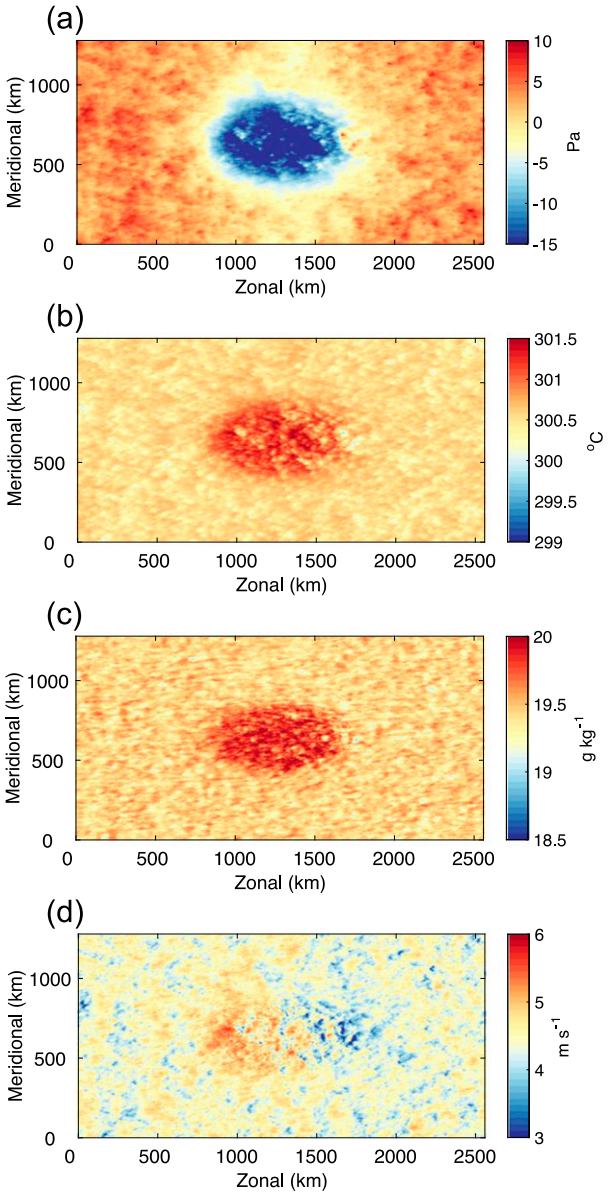


FIG. 9. Surface time-averaged (a) pressure, (b) air temperature, (c) specific humidity, and (d) $u$ component of velocity for case U6. Time averaging is over the first 12 h of day 1 from 15-min snapshots.

the boundary layer consistent with the hydrostatic pressure-induced boundary layer convergence mechanism (e.g., Lindzen and Nigam 1987), but does not represent an equilibrium state with fully developed convection as in other studies linking global-scale tropical SST and rainfall variability (e.g., Back and Bretherton 2009).

The surface wind fields *after* deep convection has formed (Figs. 13c,d) do not correspond to the warm patch pressure signal shown in Figs. 9 and 10. Instead, convection generates a much stronger, complex perturbation pressure field dominated by cold pools and midlevel latent heating. The direct influence of the SST patch is greatly reduced after the initial 12 h.

### c. *Low winds and small SST variations*

Overall, our experiments suggest that lower wind speeds lead to a more pronounced influence of SST anomalies on convective development. Two experiments with a warm patch $\Delta T = 1$°C SST and winds of 6 and 12 m s$^{-1}$ (cases U6-1 and U12-1F, respectively), and a single experiment with $\Delta T = 0.5$°C SST and a wind of 3 m s$^{-1}$ (case U3) were conducted to test this hypothesis. Hovmöller plots of meridionally averaged rainfall shown in Fig. 14 for these scenarios demonstrate that even with weak SST perturbations, convection is enhanced by warmer surface waters with weak winds. Winds of 12 m s$^{-1}$ with a fixed 1°C SST anomaly (Fig. 14c) produce only a small convective enhancement in response to the fixed SST anomaly, suggesting that even without ocean mixing, strong winds smooth out the enhanced MSE associated with small SST variations.

Plots of cloud albedo for case U3 along with SST anomaly (Fig. 15) show how a small SST anomaly generates an initial enhancement of convection followed by squall-line propagation away from the patch similar to case U6 (Fig. 2a). The mean wind in this case has a negligible effect on the convective activity. SST is affected by vertical mixing and shading of solar radiation by the clouds, but retains a warm anomaly. By the third day, convection does not cover the warm patch, again suggesting that the eventual location of convection is primarily set by the dynamics of convection rather than the SST patch location.

Although the convective response for case U3 behaves like a transient response, if the simulation is continued, convection will likely redevelop over the patch, much like the quasi-periodic convective development shown in case U6 (see Fig. 5). In general, stronger winds tend to prevent local episodic convective development. We discuss this result in more detail below.

## 4. Discussion

### a. *Flux-scale dependence*

Scale analysis of SST patch size, strength, and wind speed provides a framework for understanding how these parameters combine to enhance convection. As shown in the last section, boundary layer temperature, moisture content, and feedback from convective heat release can generate reduced local surface pressure and preferred regions of deep convective development.

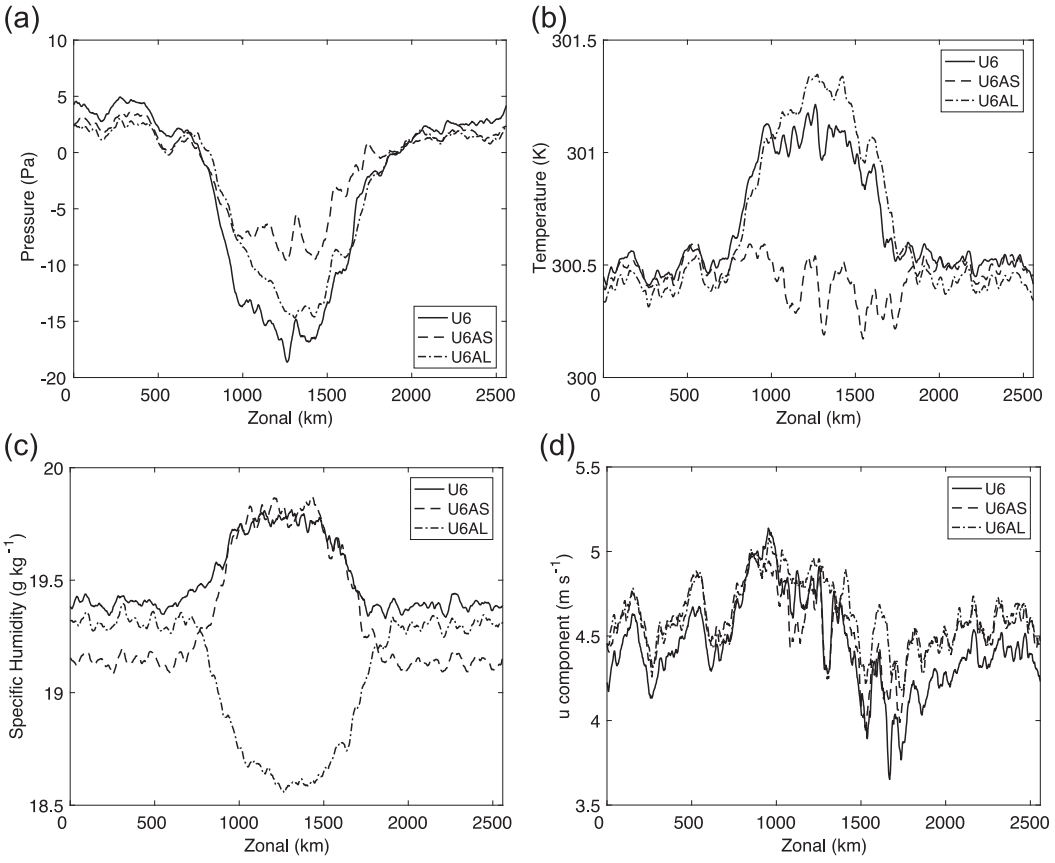


FIG. 10. Surface time- and meridional-averaged (a) pressure, (b) temperature, (c) specific humidity, and (d) $u$ component of velocity for cases U6, U6AS, and U6AL. Time averaging is over the first 12 h from day 1 using 15-min snapshots. Meridional averaging is between $y = 500$ and 780 km, centered on the warm patch.

Fluxes are scaled by the wind speed and sea–air temperature and humidity difference, according to the bulk aerodynamic flux formulation,

$$F_s \sim U\Delta T; \quad F_l \sim U\Delta q,$$

where $\Delta T$ is the difference between the air temperature and the SST, $\Delta q$ is the difference between the surface specific humidity and the saturation specific humidity at the SST, and $U$ represents the surface wind speed. Fluxes increase with greater wind speed; however, the time that a parcel of air is over an SST patch of size $L$ decreases as wind speed increases $\delta t = L/U$. Assuming this relationship, the Lagrangian time integrated surface heat flux scales as

$$F\delta t \propto U\Delta T\delta t = \frac{U\Delta TL}{U} = \Delta TL,$$

where $\delta t$ is time scale $= L/U$. This scaling suggests that to first order the integrated turbulent surface heating is independent of wind speed.

### b. Role of wind and cold pools

For cases U6 and U3, convective squall lines propagate along the leading edge of cold pools moving upstream, away from the SST patch. Cold pools also propagate downstream, but with less intense convective development. Cases with stronger background winds, for example, case U12, do not form well-defined squall lines, most likely because cold pools are unable to overcome the stronger background advection. A simple conceptual model explains how cold pools maintain convection under different ambient wind speeds. Cold pools form when rain evaporates in downdrafts, generating a downward moving pulse of cold air that spreads laterally as shown by the outflow system in Fig. 16a. The cold pool propagates relative to the mean wind in all directions at a speed $c$, which can be approximated with shallow water theory as $c = \sqrt{g'h}$, where $g' = g\Delta\theta/\overline{\theta}$, where $g = 9.81\,\mathrm{m\,s^{-2}}$, $\Delta\theta$ is the cold pool temperature departure from the mean boundary layer temperature $\overline{\theta}$, and $h$ is the cold pool depth. We view the velocity structure relative to the background

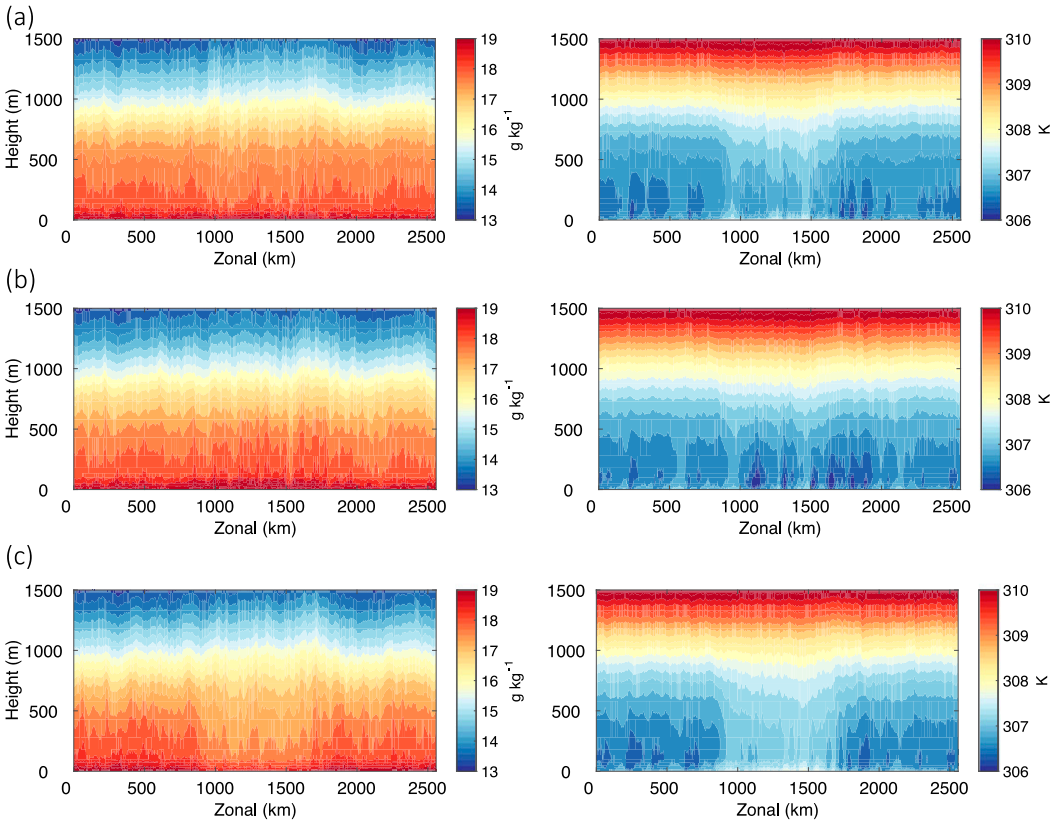


FIG. 11. (left) Specific humidity and (right) potential temperature at $y = 640$ km averaged over the first 12 h of day 1 using 15-min snapshots from case (a) U6, (b) U6AS, and (c) U6AL.

flow $U$ (Fig. 16a). The cold pool decreases the flow upstream of the cold pool center and increases the flow downstream from the center. We note that vertical shear of the background wind is weak in the model boundary layer over the depths of cold pools (Fig. 4) and the ambient wind in the boundary layer is nearly equal to $U$.

New convection is often generated in the region of strong convergence near the edge of expanding cold pools and can be identified in Hovmöller diagrams by linear features or characteristics as shown schematically in Figs. 16b and 16c. We are interested in convection that appears to travel at $U \pm c$. Assuming new convection is tied to cold pool fronts, then we expect rainfall to have characteristic propagation speeds that follow the shifted velocity field (Fig. 16b).

In the absence of background winds, convergence and the formation of new convection is produced along the leading edge of the cold pool. Background wind produces asymmetry in the upstream and downstream sections of the cold pool with weaker wind speed upstream from the cold pool center and stronger surface wind speed downstream from the center as shown in Fig. 16a. For example, in the U6 case shown in Fig. 16c the cold pool propagation speed $c = \sim 7\,\mathrm{m\,s^{-1}}$ (for a cold pool with $h = \sim 500$ m and a temperature $\sim 3$ K colder than the background boundary layer) and the boundary layer wind speed is $\sim 5\,\mathrm{m\,s^{-1}}$. The leading edge of cold pools in this case are moving about $-2\,\mathrm{m\,s^{-1}}$ in the upstream direction and $10\,\mathrm{m\,s^{-1}}$ in the downstream direction as shown schematically in Fig. 16c. Applying a similar cold pool propagation speed for case U12 predicts that new convection from upstream-traveling cold pools nevertheless moves downstream relative to the warm patch, which may explain why convection shown in Fig. 6 for U12 is less organized.

### c. *Surface drag effects on cold pools*

Our results indicate that background wind, without significant shear, affects the symmetry of cold pools and near-surface convergence associated with cold pool fronts. Romps and Jeevanjee (2016) analyzed the dynamics of simple, axisymmetric cold pools without background winds, and determined that the dominant term in reducing cold pool momentum was related to the entrainment rate along the top of the cold pool.

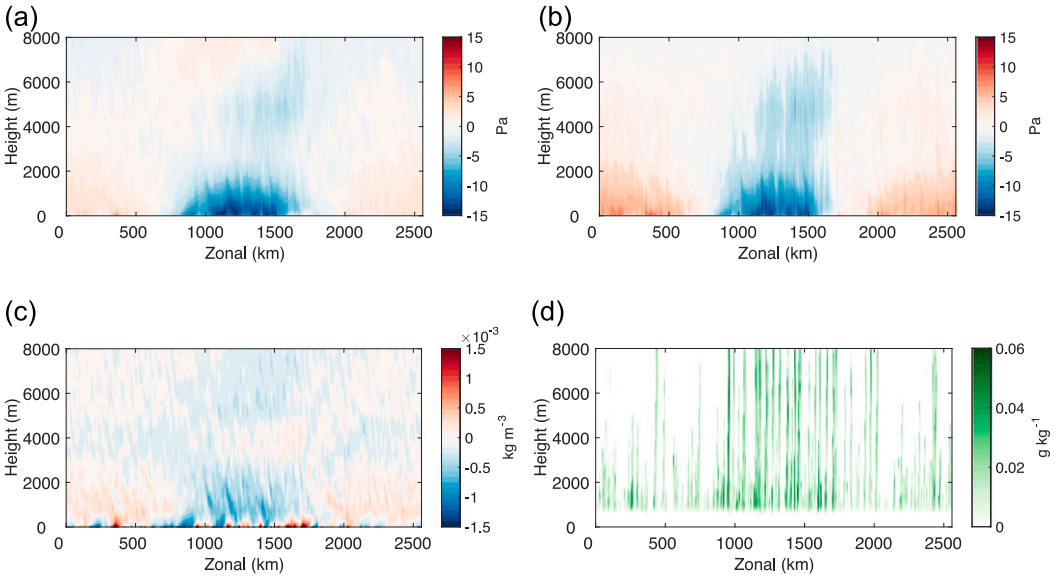


FIG. 12. Vertical cross sections of perturbation (a) pressure, (b) hydrostatic pressure, and (c) density, along with (d) cloud water mixing ratio from case U6AS averaged over the first 12 h of the simulation. Perturbations are calculated by removing the zonal mean.

Surface drag in their analysis was of lesser importance. In our experiments, addition of background wind alters the surface drag on the upstream and downstream portions of the cold pool, while entrainment is not affected to first order. Surface drag is proportional to the surface velocity squared, which as shown in Fig. 16a is reduced on the upstream (left) side of the cold pool, and increased on the downstream (right) side of the cold pool. As an example, for case U6 the effective cold pool upstream surface velocity is $\sim 1\,\mathrm{m\,s^{-1}}$ versus $13\,\mathrm{m\,s^{-1}}$ on the downstream side, yielding drag that is $O(100)$ times larger for the downwind-propagating section of the cold pool. Because of this asymmetry, we hypothesize that winds on the downstream section of cold pools (right side of Fig. 16a) lose more momentum and dissipate more rapidly, compared to winds on the upstream section (left side of Fig. 16a), thereby reducing downstream convergence. In contrast, the upstream side of

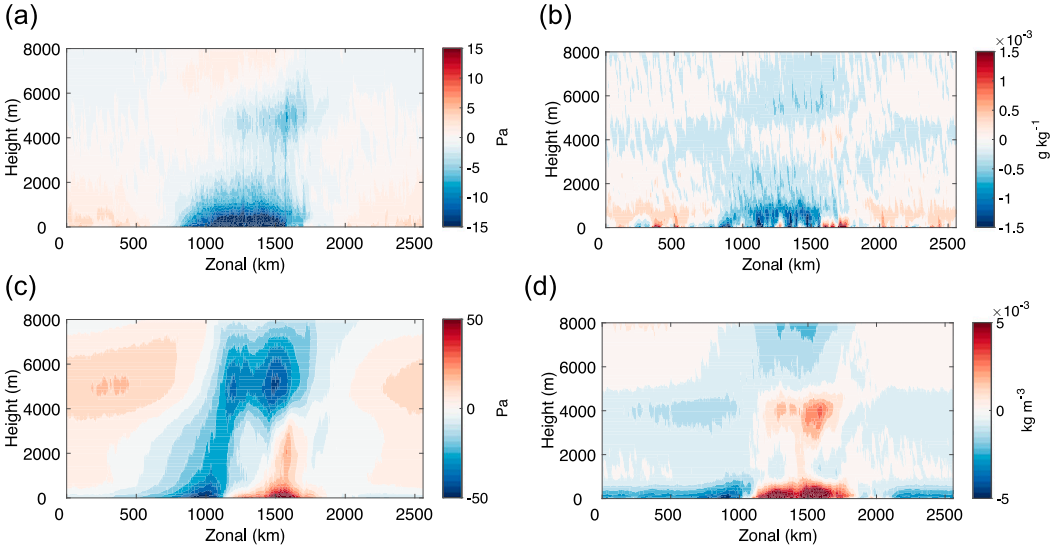


FIG. 13. Vertical cross sections of perturbation (a) pressure, (b) density from case U6 averaged over the first 12 h, and (c) pressure and (d) density averaged between hours 12 and 24. Note the change in scale for (c) and (d).

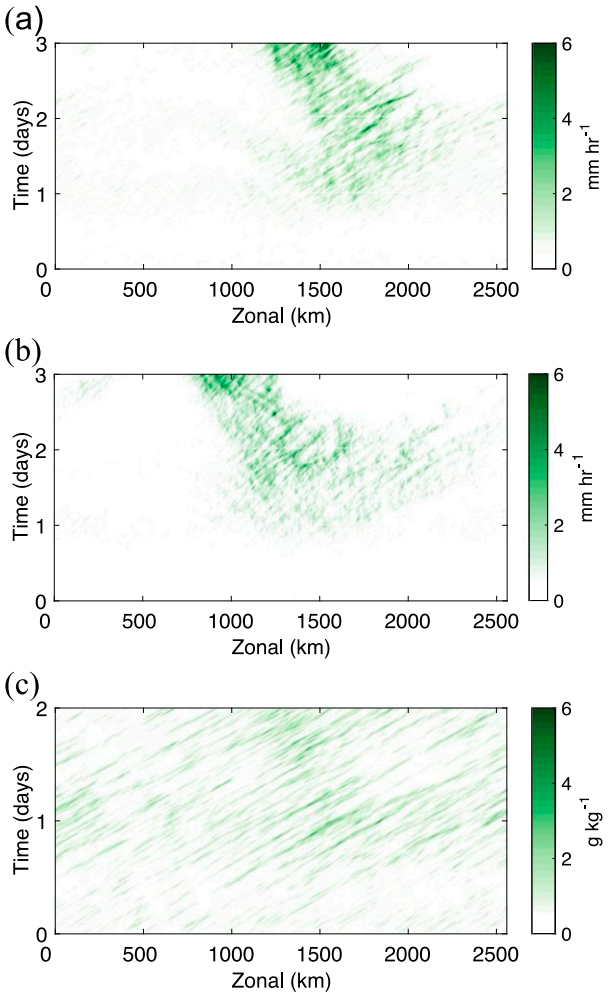


FIG. 14. As in Fig. 6a, but for cases with (a) a 1°C SST anomaly and a wind of 6 m s$^{-1}$, (b) a 0.5°C SST anomaly and a wind of 3 m s$^{-1}$, and (c) a 1°C fixed SST anomaly and a wind of 12 m s$^{-1}$.

the cold pool lasts longer and generates stronger convergence leading to new convection. This behavior is shown in Fig. 6b for case U6 where the positive velocity associated with cold, dry air sweeping downstream quickly decreases to near-background values, while the velocity perturbation persists (Fig. 6b, right side) and convection is enhanced on the upstream side of the system where surface wind speeds are near zero.

In general, we find cold pools propagate below organized lines of convection propagating away from warm SST anomalies. While stronger background wind may increase the local fluxes over the warm SST, convective cells are swept downstream of the patch and cannot develop into organized squall-line systems. Winds closer in magnitude to the cold pool propagation speed yield convective cells that are quasi stationary and can tap into the enhanced fluxes over the warm SST patch. With lower wind speeds, even small SST anomalies can enhance convective development as shown in Fig. 15, without the limiting effects of advection downstream by the ambient flow.

## 5. Conclusions

The main goal of this study was to investigate how convection organizes over mesoscale regions of warm SST anomalies in the tropical ocean. Using a cloud-resolving coupled atmosphere–mixed layer ocean model, three sets of experiments were conducted examining the response of atmospheric convection to an initial mesoscale warm SST patch. In the first set of experiments, background winds of 6 and 12 m s$^{-1}$ were prescribed and generated two different convective responses. For the 12 m s$^{-1}$ case, convection was enhanced over the warm patch, but typically propagated downwind from the warm SST center. In contrast, the 6 m s$^{-1}$ experiment developed a much stronger squall line over the warm patch that persisted for ~36 h. In both cases, the internal dynamics of the convection and convective propagation limited the duration that the convection was located over the warm patch. Experiments with fixed SST anomaly produced qualitatively similar behavior, but with stronger convective development as would be expected.

A second set of experiments determined if convective development from convergence and uplift from lower pressure tied to boundary layer warming is greater than convective development from increased moisture and heat fluxes produced by warmer SST. The importance of surface turbulent fluxes was examined by averaging either the sensible heat flux or the latent heat flux, thereby selectively removing the spatial variability associated with the warm patch. We found that for 12 m s$^{-1}$ winds, spatially averaging the latent heat flux almost eliminated convective enhancement over the warm patch. In contrast, the 6 m s$^{-1}$ case had almost no changes in the formation of convection over the patch when using either the average sensible or latent heat flux. Convergence from lower hydrostatic pressure, either from enhanced sensible heat flux, longwave flux, or the virtual temperature effect of enhanced latent heat flux and increased MSE was sufficient to maintain convection over the patch. However, the propagation of convection away from the patch during the second day of the simulation was altered by the uniform flux experiments, with nearly continuous rainfall over the patch in the case with averaged latent heat flux on days 2 and 3. Overall, we find that surface wind convergence through traditional SST forced mechanisms (e.g., Lindzen and Nigam 1987) is partially responsible for

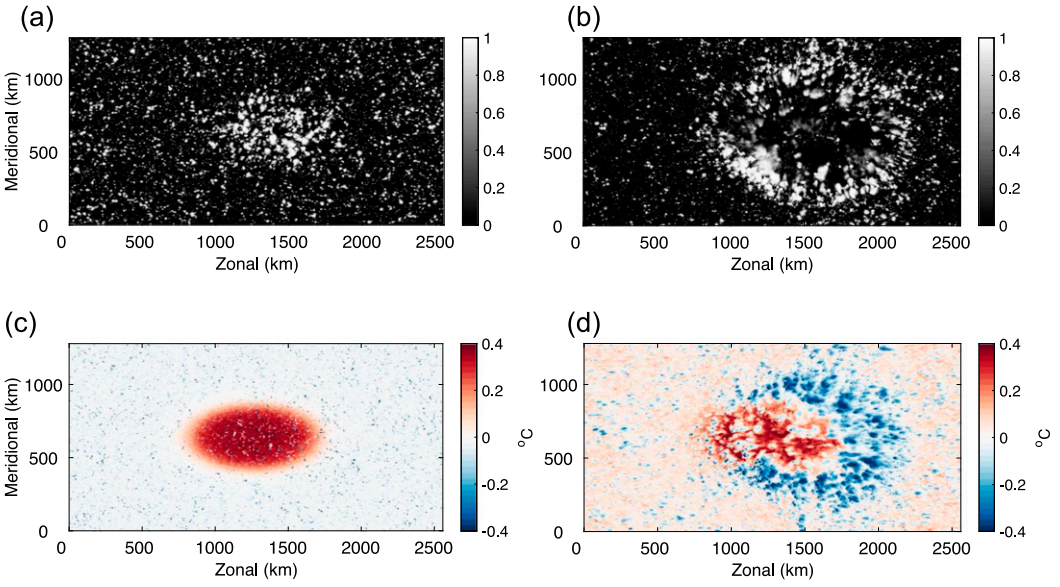


FIG. 15. (top) Cloud albedo from simulation U3 at hours (a) 48 and (b) 60 and (bottom) perturbation SST at hours (c) 48 and (d) 60. The initial SST anomaly in this experiment is 0.5°C. Perturbation SST is calculated by subtracting the average SST value and removes the diurnal variation in average SST that is of the same order as the patch anomaly.

triggering convection, but has a small role in subsequent convective activity.

Our final set of experiments, with winds of $3\,m\,s^{-1}$ and patch SST anomaly of 0.5°C, found that even small variations in SST can generate a local enhancement of convection. In contrast, the case of strong winds ($12\,m\,s^{-1}$) and a fixed 1°C anomaly generated weak convective organization. Scale analysis suggests that net heat content over a warm patch is not strongly affected by the wind speed. However, the time scale for development of convection is longer for lower winds that have weaker fluxes, leading to increased convective organization and squall-line development.

Long-lived squall lines are explained by convection tied to cold pool propagation. For background winds $<6\,m\,s^{-1}$, the cold pools (moving approximately $7\,m\,s^{-1}$) propagate upstream overtaking the background wind so that new cells are relatively stationary over the SST warm anomaly. For the $U = 12\,m\,s^{-1}$ case, even upwind-propagating cold pools are swept downstream and storms are unable to organize into consistent squall lines. Consequently, the effects of the SST anomaly are spread out over the model domain. Our results point to a list of mechanisms that can cause enhanced convection near mesoscale warm SST patches in the tropical ocean. Although the initial formation of convection by pressure convergence (as suggested by LC) is directly linked to SST, our results suggest that enhanced moist static energy flux also explains the correlation between SST and rainfall. The MSE mechanism dominates for the $U = 12\,m\,s^{-1}$ case, where density and surface pressure variations are weak. LC also determined that the correlation between SST and rainfall decreased significantly after the first 24 h, which they suggested was due to the destruction of the SST anomaly through upper-ocean cooling. In our simulations, significant SST anomalies prescribed over 10–20-m depth persist for several days. Nevertheless, convective enhancement with weak winds over the SST patch often propagates away from the patch within 24 h, which would also explain a relatively short correlation period. This behavior occurred with both active and fixed SST. In future research, we plan to investigate the response of convection to shallow warm SST anomalies, which will more directly address the decay mechanism proposed by LC.

The effect of mesoscale tropical SST variability on convection and precipitation is similar in some ways to enhancement of convection by islands (Robinson et al. 2011; Sobel et al. 2011). In both cases, surface flux variations lead to stronger convection, which then propagates and affects precipitation both locally and in the surrounding seas. Island simulations using a cloud-resolving model (Cronin et al. 2015) demonstrate convective behavior similar to our results, but with much greater precipitation intensity variation and stronger diurnal signal because of the more significant daily surface flux cycle over land. Cold pools and sea breeze circulations produce convective features

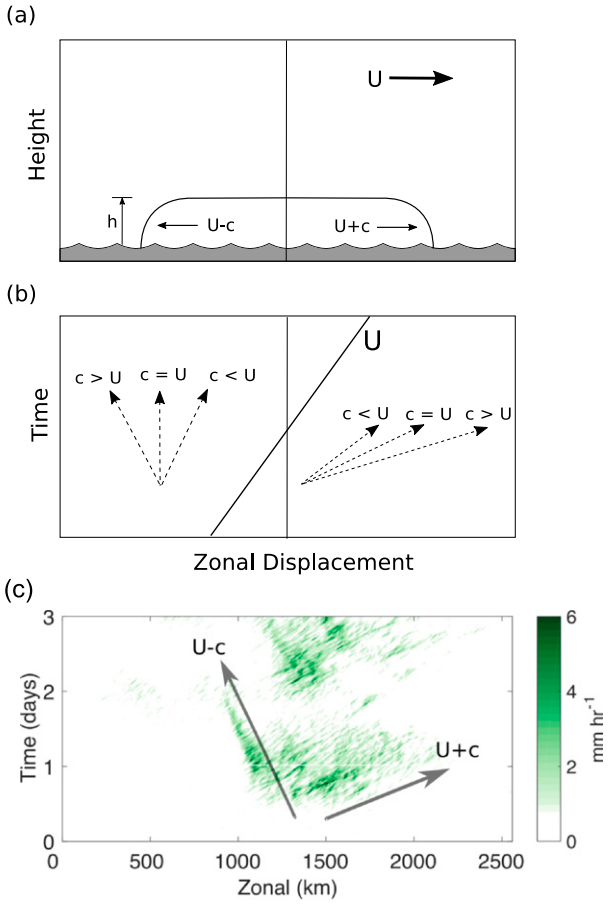


FIG. 16. (a) Schematic of a convective cold pool system, (b) Hovmöller plot of characteristics relative to a fixed point for each side of the cold pool, and (c) an example for rainfall in case U6. New convection is generated by convergence along the cold pool front and propagates with velocity *c*.

that have consistent day-to-day patterns in both time and space (Carbone et al. 2000; Wilson et al. 2001). Understanding how SST patchiness and island forcing affect larger-scale convective systems, such as the MJO, is a topic for future investigation.

*Acknowledgments.* We gratefully acknowledge the constructive comments of the three anonymous reviewers. This material is based upon research supported by the Office of Naval Research under Award N00014-15-1-2643.

## REFERENCES

Back, L. E., and C. S. Bretherton, 2009: On the relationship between SST gradients, boundary layer winds, and convergence over the tropical oceans. *J. Climate*, **22**, 4182–4196, https://doi.org/10.1175/2009JCLI2392.1.

Bellenger, H., Y. N. Takayabu, T. Ushiyama, and K. Yoneyama, 2010: Role of diurnal warm layers in the diurnal cycle of convection over the tropical Indian Ocean during MISMO. *Mon. Wea. Rev.*, **138**, 2426–2433, https://doi.org/10.1175/2010MWR3249.1.

Carbone, R. E., and Y. Li, 2015: Tropical oceanic rainfall and sea surface temperature structure: Parsing causation from correlation in the MJO. *J. Atmos. Sci.*, **72**, 2703–2718, https://doi.org/10.1175/JAS-D-14-0226.1.

——, J. Wilson, T. Keenan, and J. Hacker, 2000: Tropical island convection in the absence of significant topography. Part I: Life cycle of diurnally forced convection. *Mon. Wea. Rev.*, **128**, 3459–3480, https://doi.org/10.1175/1520-0493(2000)128<3459:TICITA>2.0.CO;2.

Colella, P., 1990: Multidimensional upwind methods for hyperbolic conservation laws. *J. Comput. Phys.*, **87**, 171–200, https://doi.org/10.1016/0021-9991(90)90233-Q.

Cronin, M. F., S.-P. Xie, and H. Hashizume, 2003: Barometric pressure variations associated with eastern Pacific tropical instability waves. *J. Climate*, **16**, 3050–3057, https://doi.org/10.1175/1520-0442(2003)016<3050:BPVAWE>2.0.CO;2.

Cronin, T. W., K. A. Emanuel, and P. Molnar, 2015: Island precipitation enhancement and the diurnal cycle in radiative-convective equilibrium. *Quart. J. Roy. Meteor. Soc.*, **141**, 1017–1034, https://doi.org/10.1002/qj.2443.

Deardorff, J. W., 1980: Stratocumulus-capped mixed layers derived from a three-dimensional model. *Bound.-Layer Meteor.*, **18**, 495–527, https://doi.org/10.1007/BF00119502.

de Szoeke, S. P., E. D. Skyllingstad, P. Zuidema, and A. S. Chandra, 2017: Cold pools and their influence on the tropical marine boundary layer. *J. Atmos. Sci.*, **74**, 1149–1168, https://doi.org/10.1175/JAS-D-16-0264.1.

Hashizume, H., S.-P. Xie, M. Fujiwara, M. Shiotani, T. Watanabe, Y. Tanimoto, W. T. Liu, and K. Takeuchi, 2002: Direct observations of atmospheric boundary layer response to slow SST variations over the eastern equatorial Pacific. *J. Climate*, **15**, 3379–3393, https://doi.org/10.1175/1520-0442(2002)015<3379:DOOABL>2.0.CO;2.

Hayes, S. P., M. J. McPhaden, and J. M. Wallace, 1989: The influence of sea surface temperatures on surface wind in the eastern equatorial Pacific: Weekly to monthly variability. *J. Climate*, **2**, 1500–1506, https://doi.org/10.1175/1520-0442(1989)002<1500:TIOSST>2.0.CO;2.

Hsu, S. A., 1984: Sea-breeze-like winds across the north wall of the Gulf Stream: An analytical model. *J. Geophys. Res.*, **89**, 2025–2028, https://doi.org/10.1029/JC089iC02p02025.

Johnson, R. H., and P. E. Ciesielski, 2013: Structure and properties of Madden–Julian oscillations deduced from DYNAMO sounding arrays. *J. Atmos. Sci.*, **70**, 3157–3179, https://doi.org/10.1175/JAS-D-13-065.1.

Kilpatrick, T. J., and S.-P. Xie, 2015: ASCAT observations of downdrafts from mesoscale convective systems. *Geophys. Res. Lett.*, **42**, 1951–1958, https://doi.org/10.1002/2015GL063025.

Large, W. G., J. C. McWilliams, and S. C. Doney, 1994: Oceanic vertical mixing: A review and a model with a nonlocal boundary layer parameterization. *Rev. Geophys.*, **32**, 363–403, https://doi.org/10.1029/94RG01872.

Li, Y., and R. E. Carbone, 2012: Excitation of rainfall over the tropical western Pacific. *J. Atmos. Sci.*, **69**, 2983–2994, https://doi.org/10.1175/JAS-D-11-0245.1.

Lindzen, R. S., and S. Nigam, 1987: On the role of sea surface temperature gradients in forcing low-level winds and convergence in the tropics. *J. Atmos. Sci.*, **44**, 2418–2436, https://doi.org/10.1175/1520-0469(1987)044<2418:OTROSS>2.0.CO;2.

Liu, C., and M. W. Moncrieff, 1998: A numerical study of the diurnal cycle of tropical oceanic convection. *J. Atmos. Sci.*, **55**, 2329–2344, https://doi.org/10.1175/1520-0469(1998)055<2329:ANSOTD>2.0.CO;2.

Mason, P. J., 1994: Large-eddy simulation: A critical review of the technique. *Quart. J. Roy. Meteor. Soc.*, **120**, 1–26, https://doi.org/10.1002/qj.49712051503.

Mlawer, E. J., S. J. Taubman, P. D. Brown, M. J. Iacono, and S. A. Clough, 1997: Radiative transfer for inhomogeneous atmosphere: RRTM, a validated correlated-k model for the longwave. *J. Geophys. Res.*, **102**, 16 663–16 682, https://doi.org/10.1029/97JD00237.

Moum, J. N., and Coauthors, 2014: Air–sea interactions from westerly wind bursts during the November 2011 MJO in the Indian Ocean. *Bull. Amer. Meteor. Soc.*, **95**, 1185–1199, https://doi.org/10.1175/BAMS-D-12-00225.1.

Robinson, F. J., S. C. Sherwood, D. Gerstle, C. Liu, and D. J. Kirshbaum, 2011: Exploring the land–ocean contrast in convective vigor using islands. *J. Atmos. Sci.*, **68**, 602–618, https://doi.org/10.1175/2010JAS3558.1.

Romps, D. M., and N. Jeevanjee, 2016: On the sizes and lifetimes of cold pools. *Quart. J. Roy. Meteor. Soc.*, **142**, 1517–1527, https://doi.org/10.1002/qj.2754.

Samelson, R., E. D. Skyllingstad, D. B. Chelton, S. K. Esbensen, L. W. O'Neill, and N. Thum, 2006: A note on the coupling of wind stress and sea surface temperature. *J. Climate*, **19**, 1557–1566, https://doi.org/10.1175/JCLI3682.1.

Skyllingstad, E. D., and S. P. de Szoeke, 2015: Cloud-resolving large-eddy simulation of tropical convective development and surface fluxes. *Mon. Wea. Rev.*, **143**, 2441–2458, https://doi.org/10.1175/MWR-D-14-00247.1.

Sobel, A. H., C. D. Burleyson, and S. E. Yuter, 2011: Rain on small tropical islands. *J. Geophys. Res.*, **116**, D08102, https://doi.org/10.1029/2010JD014695.

Thompson, G., P. R. Field, R. M. Rasmussen, and W. D. Hall, 2008: Explicit forecasts of winter precipitation using an improved bulk microphysics scheme. Part II: Implementation of a new snow parameterization. *Mon. Wea. Rev.*, **136**, 5095–5115, https://doi.org/10.1175/2008MWR2387.1.

Tulich, S. N., and B. E. Mapes, 2008: Multiscale convective wave disturbances in the tropics: Insights from a two-dimensional cloud-resolving model. *J. Atmos. Sci.*, **65**, 140–155, https://doi.org/10.1175/2007JAS2353.1.

Vickers, D., and L. Mahrt, 2006: Evaluation of the air-sea bulk formula and sea-surface temperature variability from observations. *J. Geophys. Res.*, **111**, C05002, https://doi.org/10.1029/2005JC003323.

Wicker, L. J., 2009: A two-step Adams–Bashforth–Moulton split-explicit integrator for compressible atmospheric models. *Mon. Wea. Rev.*, **137**, 3588–3595, https://doi.org/10.1175/2009MWR2838.1.

Wilson, J. W., R. E. Carbone, J. D. Tuttle, and T. D. Keenan, 2001: Tropical island convection in the absence of significant topography. Part II: Nowcasting storm evolution. *Mon. Wea. Rev.*, **129**, 1637–1655, https://doi.org/10.1175/1520-0493(2001)129<1637:TICITA>2.0.CO;2.